https://doi.org/10.5194/egusphere-2026-1907
Preprint. Discussion started: 18 May 2026

Multi-sensor tracking of pyroconvection reveals discrepancies between satellite cloud-top detection and convective dynamics

Adrien Guyot[1,2], Jacob Vile[2,3], Louis Soulard-Fischer[1,4], Hamish McGowan[2], Alain Protat[1], Caroline Poulsen[1]

[1] Australian Bureau of Meteorology, Melbourne, Australia

[2] Weather and Climate Science Research Alliance, The University of Queensland, Brisbane, Australia

[3] University of Albany, State University of New York (SUNY), New York, USA

[4] Météo-France, Toulouse, France

Correspondence to: Adrien Guyot (a.guyot@uq.edu.au)

Abstract. Clouds generated by intense wildfires can evolve from pyrocumulus (pyroCu) to pyrocumulonimbus (pyroCb), injecting smoke into the upper troposphere and occasionally the stratosphere. Automated satellite-based detection of pyroCb is therefore critical for monitoring extreme fire–atmosphere interactions, yet such approaches inherently rely on cloud-top properties rather than the underlying convective dynamics.

Here, we evaluate the pyroCb detection algorithm of Peterson et al. (2017), originally developed for GOES observations over North America, in the Australian context using Himawari-8 multispectral imagery during the 2019–2020 Black Summer bushfires. Satellite-derived classifications are assessed against independent observations from operational weather radar and total lightning networks within a multi-sensor framework implemented in the PyroScope platform. An object-based tracking approach is used to compare the temporal evolution of radar- and satellite-derived pyroconvective features.

Satellite observations reliably capture the onset of deep pyroconvective development, showing strong agreement with radar-derived echo-top heights and lightning activity during the early phase. However, a systematic divergence emerges as events evolve, with satellite-derived objects increasingly dominated by horizontally advected anvil structures rather than the actively convecting core. This behaviour is reflected in increasing centroid displacement, decreasing spatial overlap, and an apparent overestimation of plume extent and persistence in satellite retrievals.

https://doi.org/10.5194/egusphere-2026-1907
Preprint. Discussion started: 18 May 2026

To investigate this limitation, we introduce an additional spectral test to separate detached or decaying anvils (class 4) from intense pyroCb (class 5), and explicitly evaluate the impact of this classification on object-based metrics. Restricting the analysis to class 5 reduces the spatial extent and persistence of satellite-derived objects, but does not fully eliminate the divergence with radar observations at later stages, highlighting the inherent limitations of an anvil-based detection paradigm.

These results demonstrate that satellite-based pyroCb detection should be interpreted as a cloud-top representation of pyroconvection rather than a direct measure of the actively convecting core. Multi-sensor integration is therefore essential to distinguish between initiation, mature, and decay phases of pyroconvection. The object-based tracking framework developed here provides a foundation for future studies of pyroCb lifecycle, including the quantification of growth, decay, and potential precursors to pyroCb formation.

1. Introduction

Pyrocumulonimbus (pyroCb) clouds represent the most extreme manifestation of fire–atmosphere coupling, in which intense wildfire heat flux drives deep convection capable of penetrating the upper troposphere and, in some cases, injecting smoke into the lower stratosphere. These events have profound implications for fire behaviour, lightning generation, atmospheric composition, and radiative forcing (Potter at al., 2012a, 2012b; McRae et al., 2015). Operational detection of pyroCb has relied primarily on geostationary satellite observations (Peterson et al., 2018), which identify cold cloud tops and characteristic anvil signatures. However, satellite retrievals fundamentally sample the upper part of the cloud system, rather than the underlying convective dynamics. As illustrated schematically in Figure 1, satellite observations primarily detect cloud-top and anvil structures — including anvils that may persist after the decay of active convection — whereas weather radar directly samples the three-dimensional volumetric structure of the plume and convective core. This distinction between a cloud-top framework and a dynamical-core framework underpins the central question addressed in this study: to what extent do satellite-based pyroCb detections correspond to actively convecting fire-driven storms?

https://doi.org/10.5194/egusphere-2026-1907
Preprint. Discussion started: 18 May 2026

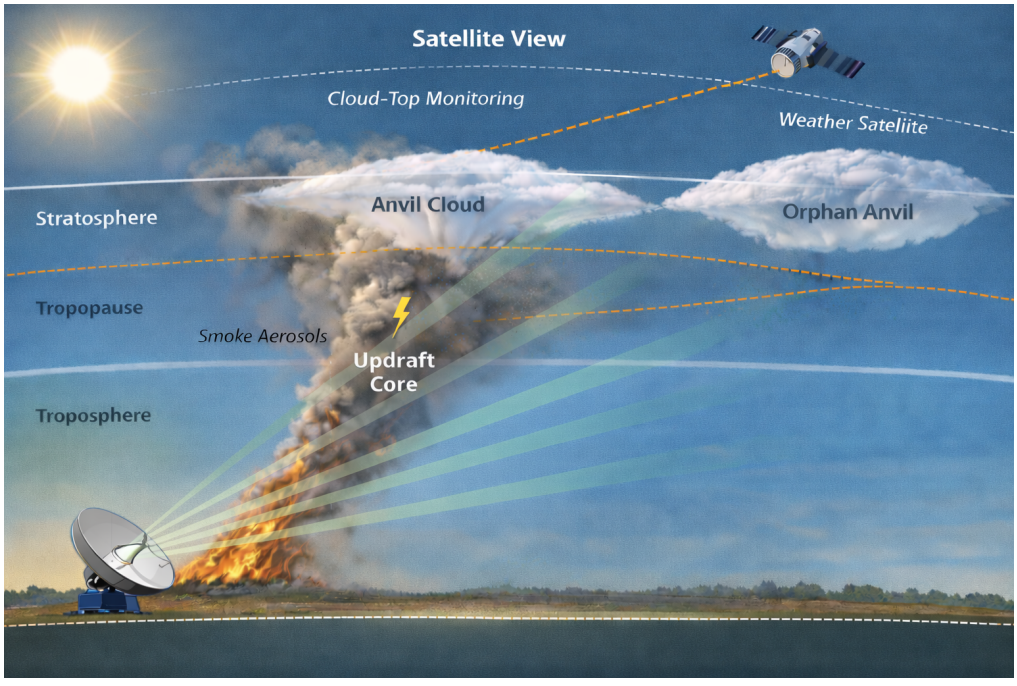

Figure 1. Conceptual schematic of pyroCb observational geometry. Geostationary satellite retrievals primarily detect cold cloud tops and anvils (including orphan anvils detached from active convection), whereas weather radar samples the volumetric structure of the plume and convective core. Radar beams broaden with range and intersect different altitudes depending on elevation angle.

The 2019–2020 Australian "Black Summer" bushfires provided an unprecedented example of extreme pyroconvection. Approximately 24 million hectares burned nationwide, including over 5.5 million hectares in New South Wales alone (Nolan et al., 2021). During this period, 38 documented pyroCb pulses occurred within two major outbreaks in late December 2019 and early January 2020 (Peterson et al., 2021) (Figure 2). The resulting smoke injection into the lower and mid-stratosphere was comparable in magnitude to that of major volcanic eruptions and persisted for over three months, contributing to measurable perturbations in atmospheric composition and circulation (Schwartz et al., 2020; Ohneiser et al., 2022). These events highlight the need for reliable and early detection and monitoring of pyroCb, both for scientific understanding and operational wildfire management.

Despite the increasing attention given to pyroCb, their definition depends strongly on the observational framework employed. From a dynamical and microphysical perspective, pyroCb are deep convective systems triggered or enhanced by wildfire heat fluxes, characterised by strong updrafts, mixed-phase microphysics, lightning production, and, in extreme cases, tropopause penetration (Rosenfeld et al., 2007; Peterson et al., 2017b). Radar observations can resolve the vertical development of these systems through echo top heights (ETH), Doppler velocities indicative of strong vertical motion, and polarimetric signatures

https://doi.org/10.5194/egusphere-2026-1907
Preprint. Discussion started: 18 May 2026

associated with graupel, hail, and mixed-phase hydrometeors (McRae et al., 2015; McCarthy et al., 2019). Lightning detection networks provide further confirmation of electrification linked to vigorous convection.

In contrast, satellite-based identification relies primarily on cloud-top properties. Geostationary sensors detect cold cloud tops using thermal infrared channels and assess cloud opacity and phase using split-window brightness temperature differences (Inoue, 1987). Within this framework, the presence of a glaciated anvil cloud becomes a central diagnostic feature. A pyroCb is therefore often defined operationally by the appearance of a cold, optically thick anvil with a distinct microphysical signature in shortwave infrared channels, frequently combined with evidence of lightning activity and association with an underlying fire hotspot. While effective for large-scale monitoring, this approach implicitly assumes that cloud-top anvil characteristics provide a reliable proxy for the location of the active deep convection beneath.

Peterson et al. (2017a; hereafter P17) developed the first automated algorithm for detecting intense pyroconvection using daytime infrared observations from GOES over western North America. The algorithm applies a sequence of tests: (i) identification of deep convection based on cloud-top brightness temperature; (ii) discrimination between pyroconvective and non-pyroconvective storms using the brightness temperature difference between 3.9 μm and 11 μm, reflecting the distinct microphysical signature of pyroCb anvils; and (iii) a cloud opacity test based on split-window infrared channels to exclude thin cloud edges and false positives. This framework has since been applied to extend pyroCb inventories in North America (Peterson et al., 2017a), to characterise the Black Summer outbreak (Peterson et al., 2021), and to assess global pyroCb occurrence (Fromm et al., 2022).

However, the P17 algorithm was developed and tuned for North American conditions and GOES spectral characteristics. Its performance in other geographic and climatic contexts remains insufficiently assessed. Moreover, while the algorithm has been evaluated against curated pyroCb archives and satellite imagery, few studies have systematically compared its classifications with independent dynamical observations such as radar-derived cloud heights, polarimetric signatures, and lightning density. This gap is important because satellite-based detection is inherently cloud-top focused. As pyroCb mature, their anvils can advect and persist long after the convective core has weakened or dissipated. If detection relies primarily on anvil properties, detached or “orphan” anvils may be misclassified as ongoing intense pyroconvection despite the absence of active updrafts or electrification beneath. Whether this represents a minor artefact or a structural limitation of satellite-only detection has implications for pyroCb climatologies and estimates of stratospheric smoke injection frequency.

Recent work has demonstrated that cloud-top motion derived from geostationary satellite imagery can provide quantitative insight into pyroCb updraft dynamics using optical flow techniques, capturing convective pulses and variations in updraft strength (McHardy et al., 2024). However, these approaches remain limited to cloud-top observations and do not directly resolve the underlying convective structure.

https://doi.org/10.5194/egusphere-2026-1907
Preprint. Discussion started: 18 May 2026

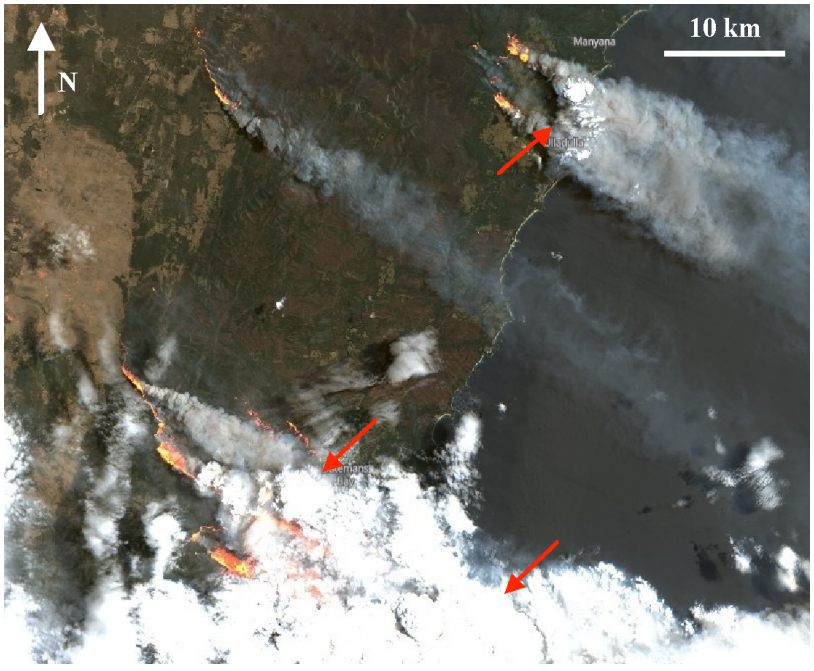

Figure 2. Pyroconvective clouds (marked with red arrow) on the 31st of December 2019 on the New South Wales coast. RGB composite image created from Sentinel 2 imagery with sur-imposed fire hot spots using a sentinel custom script Hub [https://www.sentinel-hub.com, last accessed 27 February 2026].

Australia provides an ideal setting to evaluate these questions. The Black Summer bushfires generated numerous pyroconvective events within range of operational weather radars operated by the Australian Bureau of Meteorology, including dual-polarimetric systems capable of resolving hydrometeor phase and microphysical structure. Concurrently, the Advanced Himawari Imager (AHI) onboard the Japanese Himawari-8 geostationary satellite provides multispectral imagery comparable to GOES, enabling adaptation of the P17 detection framework to the Australian region. The availability of lightning data from national total lightning networks (Kaplan and Lau 2022; Zhu et al., 2022) and numerical weather prediction (NWP) outputs further allows a multi-sensor assessment of pyroconvective development.

In this study, we implement and adapt the P17 pyroCb detection algorithm using Himawari-8 observations during selected events of the 2019–2020 Australian bushfire season. We apply parallax correction to improve spatial alignment between satellite and radar observations and evaluate the timing and spatial extent of satellite-derived classifications against radar-derived echo top heights and lightning activity. Particular attention is given to cases where satellite retrievals identify intense pyroconvection in the absence of radar-detected deep convection, with the aim of diagnosing systematic behaviours related to advected or detached anvils. We further test a modified spectral criterion designed to reduce false identification of such orphan anvils.

https://doi.org/10.5194/egusphere-2026-1907
Preprint. Discussion started: 18 May 2026

To facilitate this analysis, we developed PyroScope, a Python-based multi-sensor platform that integrates geostationary satellite data, NWP products, radar volumes, and lightning observations on a common grid and time framework. This platform enables consistent cross-comparison of satellite-based classifications with independent dynamical diagnostics and supports reproducible evaluation of algorithm performance.

By combining geostationary satellite observations with radar and lightning data, this study provides an independent assessment of satellite-based pyroCb detection in the Australian context. Beyond algorithm evaluation, the objective is to quantify how satellite-derived classifications relate to the dynamical evolution of pyroconvective systems, and to determine to what extent an anvil-based detection framework captures the lifecycle of active convection.

2. Methods

2.1 Satellite data

The Himawari suite of geostationary satellites are operated by the Japan Meteorological Agency (JMA). The AHI onboard the satellite platform provides high-resolution imagery over the Asia-Pacific region. The current operational satellite is Himawari-9 while Himawari-8 was the operational satellite for the 2019-2020 wildfires. They are positioned at 140.7°E longitude, and capture data every 10 minutes across 16 spectral bands (3 visible, 3 near-infrared, and 10 infrared) with a spatial resolution ranging from 0.5 to 2 km at nadir, depending on the band. In this paper, we selected pyroCb cases from the 2019-2020 Australian Black Summer bushfires from November 2019 to January 2020, and from 2023, when Himawari 8 was operational.

Himawari-8 operates in slightly different bands than GOES, therefore we used slightly different bands than that used in P17. Himawari-8 band 7 at 3.9 μm (shortwave infrared) was used instead of the band 7 of GOES (at 4.0 μm). This band is typically used for characterising cloud properties and low-level cloud formation due to its sensitivity to temperature variations. It is also used for the detection of wildfire or hot spots, and to derive fire radiative power (FRP) (Xu et al., 2017). Here it is used for the cloud microphysics test from P17 algorithm that is described in detail further below. Himawari-8 band 14 at 11.2 μm was used instead of the 11.0 μm band 4 of GOES satellite. This band is primarily used for monitoring cloud top temperatures, due to its strong sensitivity to thermal radiation. Unlike the shortwave bands, 11.2 μm is less affected by atmospheric moisture, making it effective for clear-sky temperature observations, such as detecting cold cloud tops in storms. Himawari-8 band 16 at 13.3 μm is in the longwave infrared spectrum, and is used here instead of the 13.0 μm of GOES. This wavelength is particularly sensitive to CO_2 absorption and is mostly used for upper-level atmospheric temperature estimation, such as high clouds to determine their altitude. In the P17 algorithm, it is used to determine cloud opacity. We note that the small differences in

https://doi.org/10.5194/egusphere-2026-1907
Preprint. Discussion started: 18 May 2026

bandwidth can slightly affect the threshold tests in the P17 algorithm and might require different values to be used for Himawari. We did not conduct such a test in this study.

2.2 A new modified version of the P17 algorithm

The P17 algorithm is run on a pixel per pixel basis, and does not consider relationships between pixels. It consists of three consecutive tests: (1) first, the algorithm identifies which pixels can be associated to deep convection – including traditional (non-wildfire forced) convection; (2), then the traditional convection is separated from the pyro-convection using the particular microphysical signature of pyroCb; (3) the final test evaluates if the detected convection is optically thick.

Deep convection is detected based on the brightness temperature at 11.2 µm (hereafter denoted as BT_{11}). P17 utilises a threshold of BT_{11} of less than – 20°C for identifying deep convection, with $-35°C < BT_{11} < -20°C$ being associated to marginal convection – including deep non-ice or mixed phase clouds that do not reach the tropopause. P17 utilises the threshold of $BT_{11} < -35°C$ for identifying intense pyroCb, a value slightly lower than −38°C given by Rosenfeld et al. (2007) to account for averaging subpixel convection. As noted by P17, criteria on BT_{11} alone are not sufficient to detect pyroCb as it also includes traditional convection. Therefore, the second test utilises the characteristic microphysical signature of pyroCb.

The second test of the algorithm focuses on the detection of cloud optical thickness. P17 introduces this test to dismiss pixels that trigger a false positive in the previous test due to high values of $BT_{3.9}$ created by strong signals below translucent clouds. This test takes advantage of the fact that PyroCb are very opaque clouds, unlike these false positive edge pixels. P17 utilises differences in brightness temperatures (also known as “split-window”) between 11.0 µm and 13.0 µm. Because most research was done on previous versions of GOES, there was no consensus on which threshold value to use for the classification of opaque clouds at the newer wavelengths of GOES. Thus, P17 conducted a sensitivity analysis on a few pyroCb cases and settled on a threshold value of 3.0°C. Pixels showing differences between 11.0 µm and 13.0 µm bands below that threshold were classified as cloud-edge pixels, while pixels above this threshold would correspond to pyroCb. Himawari-8 has a 12.4 µm band, therefore it is possible to use either or both split windows between 11.2 µm and 12.4 µm, and 11.2 µm and 13.3 µm. We decided to conduct a sensitivity analysis to: (1) the type of split window; (2) the threshold value for the difference between 11.2 µm and 13.3 µm ($BT_{11.2}$ - $BT_{13.3}$).

The core idea of the P17 pyroCb detection algorithm resides in its microphysical test. It uses the fact that pyroCb are characterised by anvil clouds with relatively smaller droplets and ice particles compared to anvils from traditional cumulonimbus (Rosenfeld et al., 2007). This is reflected in the values of the brightness temperature at 3.9 µm ($BT_{3.9}$) where the small cloud droplets and ice will reflect more of the sunlight during daytime and increase the value of $BT_{3.9}$ for pyroCb

https://doi.org/10.5194/egusphere-2026-1907
Preprint. Discussion started: 18 May 2026

anvils. P17 uses the difference between $BT_{3.9}$ and BT_{11} to quantify this signature, where the larger differences are attributed to the presence of a pyroCb cloud. P17 utilises two conditional tests and thresholds: (i) an initial test looks at differences between $BT_{3.9}$ and BT_{11} larger than 50°C as a criterion for pyroCb classification; (ii) a second test uses a higher threshold of 60°C for situations with high cloud base, defined as Lifting Condensation Level (LCL) temperature < 0°C or LCL height > 3000 m above ground level (AGL). P17 implements this additional test using the LCL to account for convection forming in inland regions of North America with higher cloud bases, and therefore traditional convection may produce false positives with similar microphysics as pyroCb under these conditions. P17 notes that this additional test is used to increase confidence in retrievals but is not strictly necessary. Given the importance of this microphysical test in the algorithm and the regional specificity of the Northern American cases, we decided to explore the sensitivity of P17 retrievals to these thresholds on the difference between $BT_{3.9}$ and BT_{11} for the Australian cases selected in this paper. P17 also utilises a condition on the solar zenith angle (SZA) to be below 75° to avoid specular reflection effects that affects accuracy of the difference between $BT_{3.9}$ and BT_{11}. Peterson mentions that this effect was observed to be more pronounced in Canada at sunrise as this is a region where specular reflection where the solar zenith angle and the viewing zenith angle are similar, but the further south in Australia (Tasmania) remains at relatively low latitude compared to the Northern Hemisphere events observed in North America.. An important limitation of that microphysical test, and therefore the P17 in general, is that it can only be used during daytime, as it relies on reflected light from the sun. As noted by P17, most pyroCb happen during afternoon and early evening, although there are cases of pyroCb persisting well into the night (Fromm et al., 2022), including during the 2019/2020 Black Summer bushfires. In some rare but devastating cases, pyroCb happened in the middle of the night, such as during the Black Saturday bushfires in Australia (Dowdy et al., 2017).

"Analysis periods just before sunset and after sunrise (Fig. 4, gray bars) are excluded because BTD*4–11* is unreliable (Lindsey et al. 2006). For instance, BTD*4–11* often becomes very large for cloud cover observed in Canada at sunrise. This anomaly results from specular reflection (sun glint) in areas where the solar zenith angle (SZA) and VZA are similar and the relative azimuth is high."

P17 noted that the opacity test enabled to exclude cases where the pyroCb anvil becomes advected and detached from the fire. However, based on our preliminary analysis, we found that in many instances, “orphan anvils”, disconnected from any deep convection beneath, were falsely detected as intense pyroCb (this is shown later in the results in Figures 7, 9 and 11). An additional test is thus proposed here to address this issue. It is based on the principles described in Strabala et al. (1993) who demonstrated that the 11µm minus 8 µm brightness temperature difference can inform about cloud phase, as the absorption coefficient for water increases more between 11µm and 12 µm than between 11µm minus 8 µm, while the opposite is true for ice crystals. In their work, they propose a tri-spectral combination of 8, 11 and 12 µm to estimate the cloud phase. Here, we propose to use the 8, 11 and 13 µm as we are already using the 11µm and 13 µm split window for cloud opacity. In the interest of simplicity, we are adding a single additional test using the 11 µm minus 8 µm window. For that test, we use the Himawari-

https://doi.org/10.5194/egusphere-2026-1907
Preprint. Discussion started: 18 May 2026

8 band 8.6 µm and 11.2 µm bands, and a threshold of -0.5 K to separate "orphan anvils" from the anvils connected to active pyroconvection. This condition is added as an ultimate test after the "ice cloud test" (Figure 3), and thus distinguishes two classes: Orphan pyroCb anvils, and Intense pyroCb.

Figure 3 summarises the P17 algorithm as a flowchart and shows the different labels attributed to each pixel following the succession of tests described above. There is one more class in our mask (detached or decaying anvil clouds) compared to the original P17 version: (1) absence of deep convection; (2) presence of deep convection or high thin clouds; (3) marginal (non-ice or mixed phased) pyroCb; (4) decaying or detached anvil from pyroCb; (5) intense pyroCb. The resolution of our mask is 2 km, equivalent to the coarse resolution of the infrared channels of Himawari-8.

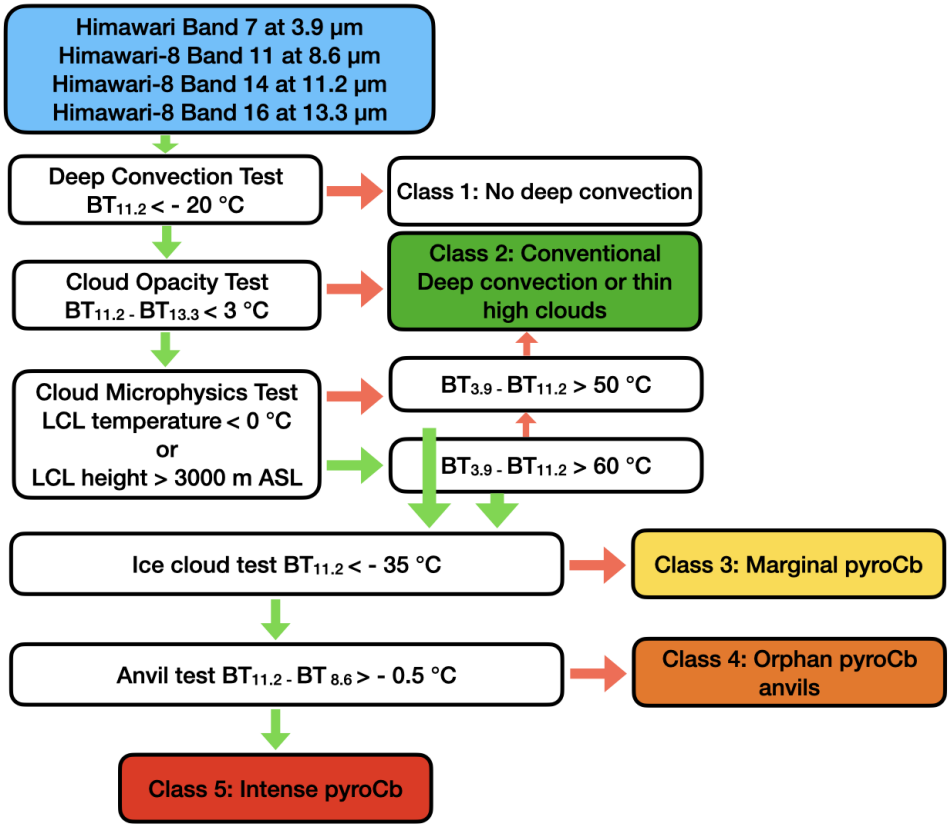

Figure 3. Flowchart of the P17 algorithm and its resulting classifications.
Adapted from Peterson et al. (2017) with modifications. Green arrows show that the algorithm progresses to the next test while orange arrows show the fall back to other classifications.

https://doi.org/10.5194/egusphere-2026-1907
Preprint. Discussion started: 18 May 2026

2.3 Parallax correction

Since one of the aims of this study is to compare satellite-derived pyroCb masks with geolocated and concomitant weather radar observations, geostationary multi-spectral imagery and satellite-derived pyroCb masks must include as few errors and uncertainties as possible. The main geolocation inaccuracy for geostationary satellites happens for high clouds for regions that are far from the satellite's nadir, either in latitude or longitude. This effect is particularly important and can artificially displace features by up to 10 km horizontally from their actual ground positions. The parallax correction was done adapting the algorithm from the publicly available package Satpy (Raspaud et al., 2025) to retrieve the shift for each pixel in X and Y based on the cloud top height. The cloud top height is routinely calculated by the Australian Bureau of Meteorology using the algorithm described in Kerdraon and Fontaine (2021), and available on the Australian National Computer Infrastructure (NCI). The correction is applied consistently to both satellite radiance fields and derived classification masks.

2.4 Radar data and selection of cases

The majority of the wildfire cases and associated clouds considered in this study are from the 2019-2020 Black Summer wildfire season, with most of the events occurring within the period ranging from 28 December 2019 till the 4 January 2020 (Petersen et al., 2021). Since the aim of this paper is to evaluate satellite-based algorithms against weather radar observations of these events, we restrict the events to within 150 km from an operational weather radar, and for periods where weather radar data, satellite data, cloud products, NWP (BARRA-2) and lightning are all available.

The Australian Bureau of Meteorology operates over 60 operational radars over the Australian continent, mostly located in the populated coastal areas. In this study, we only use horizontal reflectivity (DBZH, dBZ) to derive echo-top heights, noting that the dual polarisation moments available with some radars (Guyot et al., 2023), and the doppler velocity could provide additional proxies, and will be explored in the future. The height of clouds from weather radar observations is computed using the echo top height (ETH) method from Lakshmanan et al. (2013), where the full volumetric data is used to determine the maximum elevation angle at which a certain reflectivity threshold is exceeded. In this paper, we used the threshold value of 10 dBZ.

We used the list of pyroCb from the Australian pyroCb register (McRae, 2025) to establish a list of suitable candidates. This list (as of 30 March 2026) includes 154 events (Figure 4), from which only 22 are meeting the criteria above (Table 1). We note that several events in the list are duplicated as the same fire on the same day producing pyroCb at different intervals, so the actual number of fire events is slightly lower. All 22 pyroconvective events were investigated using the multi sensor approach described in this paper (Table 1 and Figure 4). From these 22 events, only 8 were chosen for object tracking as some events were either showing very complex multi-cell structures - thus more complex for tracking - or a very weak satellite

https://doi.org/10.5194/egusphere-2026-1907
Preprint. Discussion started: 18 May 2026

signal - therefore not meeting the objective of that paper, which was evaluating the tracking discrepancies between radar and satellite. However, these events shall be revisited in a subsequent paper to focus on the detection sensitivity and the events producing pyroconvection without transition to full pyroCb. Radars associated with each of these events (within a 150 km radius) are listed in Table 1, with the exception of the Gulf Country event from 2023 in Queensland, which was slightly further than 150 km from the radar (Richmond). This event was included nevertheless given the sheer size of the pyroCb, which produced very strong echoes even at 170 km from the radar location.

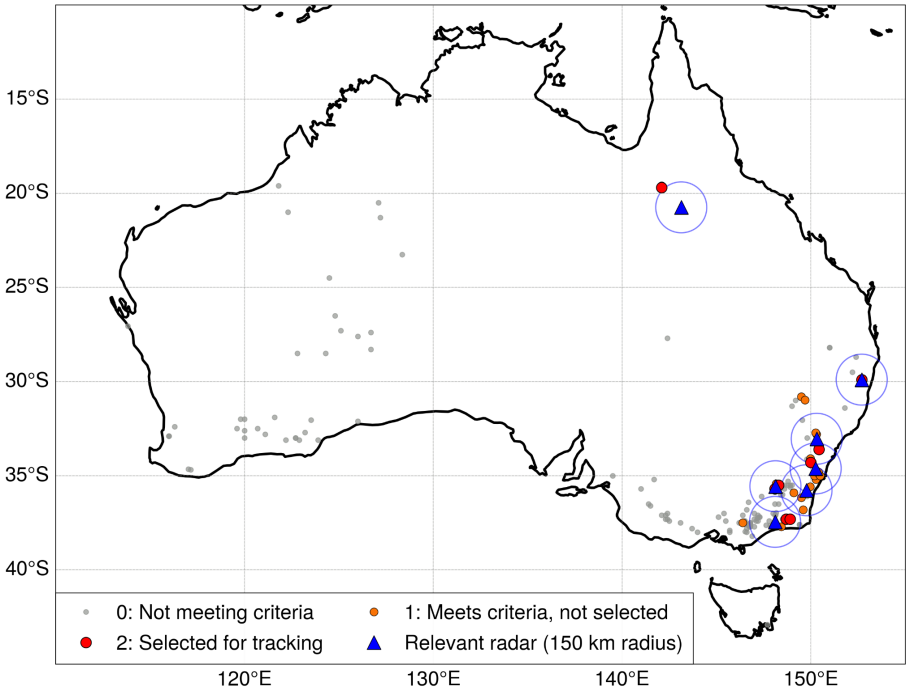

Figure 4. Geographic distribution of Australian pyroCb events (from the Australian pyroCb register maintained by McRae, 2025) and radar coverage used in this study. All known pyroCb events from the compiled database are shown, coloured according to their inclusion criteria: events not meeting data availability or proximity requirements (grey), events meeting criteria but not selected for tracking (orange), and events selected for detailed tracking analysis (red). Blue triangles indicate the locations of relevant weather radars, with circles showing their nominal 150 km range of coverage. Only radars associated with events meeting the study criteria are displayed. The selected events are concentrated in southeast Australia, reflecting both radar coverage and data availability constraints.

In summary, 154 candidate events were identified, 22 met data availability criteria, and 8 were selected for detailed tracking analysis.

https://doi.org/10.5194/egusphere-2026-1907
Preprint. Discussion started: 18 May 2026

Table 1: List of 22 pyroconvective events meeting the criteria of weather radar, satellite and lightning data availability, with wildfire front location within 150 km from an operational weather radar. NSW: New South Wales, VIC: Victoria, QLD: Queensland. From these 22 events, 8 met the criteria of strong satellite pyroCb and simple object tracking configuration.

Event	Date	Event ID	Radar (ID)	Sat detected	Tracking	Comment
Grose Valley, NSW	2019-11-22	2019_NSW_GR	Terrey Hills (71)	Strong	Y	multiple fires and multiple cells
Mt Irvine, NSW	2019-12-21	-	Terrey Hills (71)	Weak (1 pixel)	N	
Ulladulla, NSW	2019-12-21	2019_NSW_UL	Captains Flat (40)	Strong	Y	
Badja, NSW	2019-12-28	-	Captains Flat (40)	Strong	N	short lived multiple cells (complex tracking)
Mt Tianjara, NSW	2019-12-28	-	Captains Flat (40)	Strong	N	same radar and day as Badja case
Nowra, NSW	2019-12-28	-	Wollongong (3)	Strong	N	short lived multiple cells (complex tracking)
Tumut, NSW	2019-12-28	-	Wagga wagga (55)	Weak (2 pixels)	N	Short lived radar, strong lightning
Ulladulla, NSW	2019-12-28	-	Captains Flat (40)	Strong	N	Multiple cells (complex tracking)
Wombeyan caves, NSW	2019-12-29	2019_NSW_WO	Wollongong (3)	Strong	Y	Multiple cells
Goonjerah, VIC	2019-12-29	2019_VIC_GO	Bairnsdale (68)	Strong	Y	
Wulgulmerang, VIC	2019-12-30	2019_VIC_WU	Bairnsdale (68)	Strong	Y	
Nowra, NSW	2019-12-31	-	Wollongong (3)	Strong	N	Apocalyptical, multiple cells (complex tracking)

https://doi.org/10.5194/egusphere-2026-1907
Preprint. Discussion started: 18 May 2026

Yarrangobilly, NSW	2019-12-31	-	Wagga wagga (55)	Strong	N	Multiple puff of convection (complex tracking)
Nullo Mountain, NSW	2020-01-01	-	Terrey Hills (71)	no detection	N	
Cabramurra, NSW	2020-01-04	2020_NSW_CA	Wagga wagga (55)	Strong	Y	
Nowra, NSW	2020-01-04	-	Wollongong (3)	Weak (1 pixel)	N	
Mt Clear, NSW	2020-02-01	-	Captains Flat (40)	Weak (3 pixels)	N	
Tantawangalo, NSW	2020-02-01	-	Captains Flat (40)	no detection	N	
Nymboida, NSW	2023-10-25	2023_NSW_NY	Grafton (28)	Strong	Y	
Pilliga, NSW	2023-12-09	-	Namoi (69)	Weak (2 pixels)	N	
Pilliga, NSW	2023-12-18	-	Namoi (69)	no detection	N	
Gulf Country, QLD	2023-12-31	2023_QLD_GU	Richmond (107)	Very strong	Y	lowest latitude of all cases, very high Cb

2.5 Lightning data

The lightning data was sourced from the private company Weatherzone (Kaplan and Lau 2022; Zhu et al. 2022). Their total lightning network is made of sensors across Australia providing data on both intra-cloud and cloud to ground lightning strikes. Lightning density (LT, km^{-2} min^{-1}) data resolution is approximately 200 m, but this data has been re-gridded to 1 km resolution and 10 min averages.

2.7 Lifting Condensation Level (LCL)

https://doi.org/10.5194/egusphere-2026-1907
Preprint. Discussion started: 18 May 2026

As seen in section 2.2, the P17 algorithm utilises a condition on the LCL as part of its microphysical test. In our study, we compute the LCL from the Australian regional atmospheric reanalysis dataset BARRA-R2 (Su et al., 2022, 2023) that uses the Australian Bureau of Meteorology atmospheric model ACCESS to perform model hindcast and data assimilation. BARRA-R2 is available regionally at 11 km resolution. To compute the LCL, we extracted the air temperature and humidity profiles from BARRA-R2 to calculate the dew point at each pressure level. From pressure, dew point and temperature, the LCL is then calculated using the python package Metpy (May et al., 2022). The closest 11 km grid point value of the LCL to each pixel in P17 (2 km resolution) is then used in the P17 microphysical test.

2.8 Object-Based Tracking of Pyroconvective Features

Pyroconvective features were identified independently in radar and satellite fields at each analysis time step using an object-based framework. Radar objects were derived from echo-top height fields (ETH10 unless otherwise stated), thresholded at convective altitudes (≥ 8 km and ≥ 10 km, therefore creating two radar classes) and optionally constrained by reflectivity (maxZ ≥ 10 dBZ) to ensure physical relevance, while satellite objects were defined from classification outputs (e.g., P17 and G26) by selecting pixels associated with deep convection or pyroCb. This relatively low height for ETH10 is justified by the high threshold on ETH (10 dBZ) to maximise and optimise radar object detection, and account for pyroCb possibly forming at lower altitudes under higher latitudes in Victoria or Tasmania. Binary masks were constructed and contiguous regions identified via connected-component labeling, with objects below a minimum size threshold discarded. For each object, we computed area (km²) using a constant grid-cell area, centroid location (geographic coordinates), and intensity metrics including percentile-based echo-top heights (e.g., ETH10 and ETH18 at the 99.5th percentile), with percentile metrics preferred over maxima to reduce sensitivity to noise and isolated pixels. Object tracking was performed separately for radar and satellite datasets using a nearest-neighbour association between consecutive time steps, whereby candidate matches at time $t + \Delta t$ were identified based on centroid proximity and assigned using a greedy scheme minimizing centroid displacement, optionally constrained by a maximum displacement threshold to exclude physically implausible matches; unmatched objects initiated new tracks, yielding temporally consistent trajectories while maintaining methodological simplicity and robustness. At each time step, radar and satellite objects were further associated using centroid proximity to enable cross-sensor comparison, from which centroid separation distance (km), intersection-over-union (IoU) between object masks, and relative differences in object area were computed to quantify spatial agreement between radar- and satellite-derived representations.

The Intersection over Union (IoU) quantifies the spatial agreement between radar-derived and satellite-derived pyroCb detections. It is defined as:

$$IoU=|A\cap B||A\cup B|IoU=|A\cup B||A\cap B|$$

where:

https://doi.org/10.5194/egusphere-2026-1907
Preprint. Discussion started: 18 May 2026

- AA is the set of pixels classified as pyroCb by the radar,
- BB is the set of pixels classified as pyroCb by the satellite,
- |A∩B||A∩B| denotes the number of pixels where both datasets agree (intersection),
- |A∪B||A∪B| denotes the total number of pixels identified by either dataset (union).

The analysis was restricted to the early development phase of pyroconvection, defined relative to radar-detected onset, and metrics were evaluated over a fixed temporal window (e.g., 0–60 minutes from onset), during which object morphology remains relatively coherent and tracking uncertainty is minimized. Time series were derived for key variables including object area, echo-top height percentiles, and radar–satellite agreement metrics, and multi-event statistics were obtained through ensemble aggregation (e.g., median evolution). The tracking framework does not explicitly account for object splitting or merging and relies on centroid-based association, which may introduce ambiguity for elongated or rapidly evolving structures, and differences in sensor sensitivity and viewing geometry may also lead to partial mismatches between radar and satellite objects. Alternative approaches based on dense optical flow have been proposed to infer cloud-top dynamics from satellite imagery (McHardy et al., 2024), complementing object-based tracking used in this study.

Satellite-derived objects were defined using two configurations: (i) a combined definition including both class 4 (decaying or detached anvils) and class 5 (intense pyroCb), consistent with the original P17 framework, and (ii) a restricted definition using class 5 only, intended to better isolate actively convecting regions. This distinction is used to quantify the impact of classification choice on object-based tracking and radar–satellite agreement.

2.9 PyroScope: a platform for algorithm development, object tracking and evaluation

The satellite-based algorithm requires combining geostationary satellite observations together with NWP model outputs (for the estimation of the LCL). In this paper, we also use weather radar and lightning data to evaluate the relevance of satellite classifications. Ideally, all these sources of information need to be combined at the same grid resolution and for the closest timestamps. To achieve this, we decided to develop a new python-based platform named PyroScope. This dedicated software allows to: (1) define the extent of the area of interest around the fire location, and the timeframe for investigation; (2) pull all relevant data from the different sources, i.e. satellite, lightning, radar, and NWP; (3) upscale or downscale the data to the highest or lowest resolution grid; (4) perform corrections or pre-processing on the data, such as parallax correction, or gridding; (5) apply a chosen algorithm or method to the dataset; (6) identify and track object and conduct evaluation and derive metrics; (7) output the product as look up figures and all variables and products as netCDF files.

3. Results

https://doi.org/10.5194/egusphere-2026-1907
Preprint. Discussion started: 18 May 2026

3.1 Impact of Parallax Correction on Radar–Satellite Alignment

Parallax effects associated with high cloud tops can introduce significant horizontal displacement in geostationary satellite observations, affecting the spatial alignment with ground-based radar. This is particularly relevant for pyroCb, where cloud tops reach the upper troposphere or lower stratosphere.

Figure 5a shows the distribution of centroid distances between radar- and satellite-derived pyroconvective objects before and after parallax correction (the size of the objects is given in later figures 10 and 11). The correction shifts the distribution toward smaller distances, indicating improved alignment and reduced geolocation error. This is confirmed by the distribution of centroid distance changes (Δd = raw − corrected; Fig. 5b), which is dominated by positive values.

Despite this improvement, residual offsets remain. These arise from uncertainties in cloud-top height retrievals and, more fundamentally, from the difference between satellite cloud-top observations and radar sampling of the convective cores. The radar geolocation is also prone to some uncertainties, albeit of smaller magnitude than the ones related to satellites. One can expect a few km for radar-based uncertainties, due to radar geometry and projection, beam broadening, and non-uniform filling. The nature of radar scanning also affects the timing of each scan sampling, and although we optimise the smaller time difference between satellite and radar scans, there can be up to 5 min delay between the two, leading to further uncertainties in displacement between centroids. The centroid location depends on the size and shape of the objects (radar and satellite), and as a result, a much larger satellite object will have a centroid shifted compared to radar if the radar object is not located at the centre of the satellite object. As a result, parallax correction improves geometric consistency but does not fully reconcile the two observational frameworks.

https://doi.org/10.5194/egusphere-2026-1907
Preprint. Discussion started: 18 May 2026

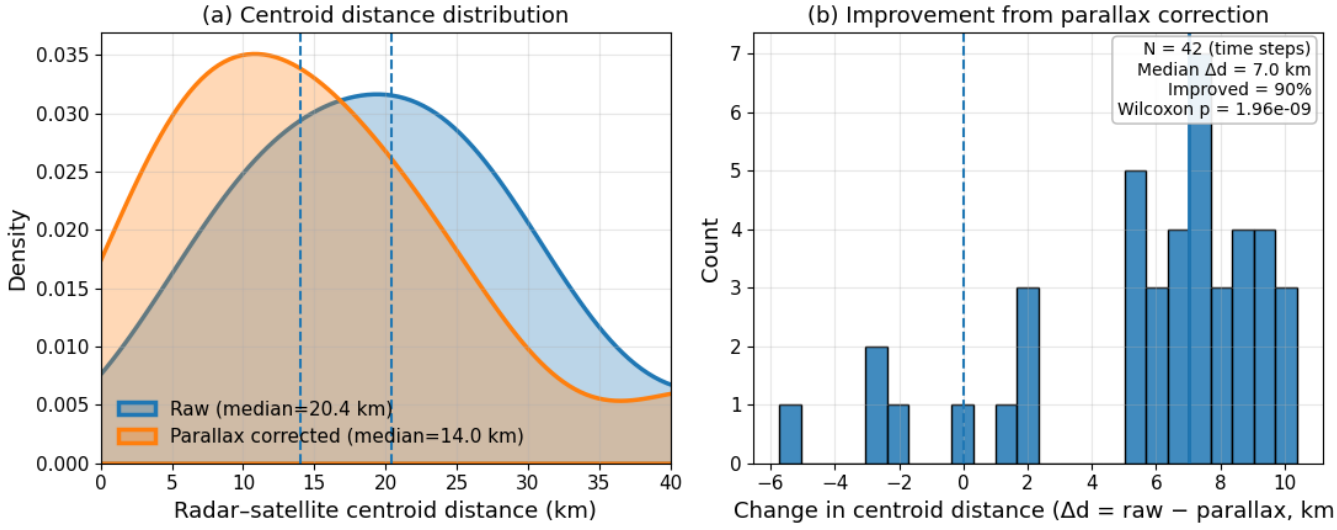

Figure 5. Impact of parallax correction on radar–satellite spatial alignment. (a) Distribution of centroid distances between radar-derived and satellite-derived pyroconvective objects before (raw) and after parallax correction, showing a systematic reduction in displacement. (b) Distribution of the change in centroid distance (Δd = raw − corrected), highlighting the overall improvement in alignment, with positive values indicating reduced separation after correction. Median distances and summary statistics are indicated in each panel.

3.2 Case Studies: Object-Based Evolution of PyroCb

3.2.1 Primary case: Gospers Mountain, NSW

The Gospers Mountain event (22 November 2019) provides a representative example of the evolution of pyroconvection and the corresponding behaviour of radar- and satellite-derived classifications. At the initial stage (02:50 UTC; Fig. 6), radar observations indicate the emergence of a compact convective core, with echo-top heights exceeding 10 km locally and co-located with the fire source. The satellite-based classification identifies a corresponding region of deep convection and pyroCb near the radar-derived object, with moderate centroid displacement (~10–15 km), the largest of the early-stage agreement observed across events studied with tracked objects, probably due to a rapid development of the pyroCb or strong wind shear at altitude. Lightning activity is already present at this stage, further supporting the interpretation of active deep convection. In feature space, pixels associated with pyroCb occupy a distinct region characterised by large $BT_{3.9}$–BT_{11} differences and cold BT_{11} values, confirming the effectiveness of the microphysical test in isolating pyroconvective signatures.

https://doi.org/10.5194/egusphere-2026-1907
Preprint. Discussion started: 18 May 2026

As the system evolves (04:10 UTC; Fig. 7), both radar and satellite observations show substantial growth in spatial extent; however, differences between the two perspectives begin to emerge. The radar-derived object remains relatively compact and anchored near the source region, while the satellite classification expands significantly downwind, reflecting the horizontal development and advection of the anvil cloud. This results in an increase in centroid displacement (exceeding ~60 km from the fire location and ~10–20 km between radar and satellite objects) and a reduction in spatial overlap. The satellite field increasingly contains regions classified as decaying pyroCb (class 4), which are spatially disconnected from the radar-observed convective core and exhibit little or no associated lightning activity.

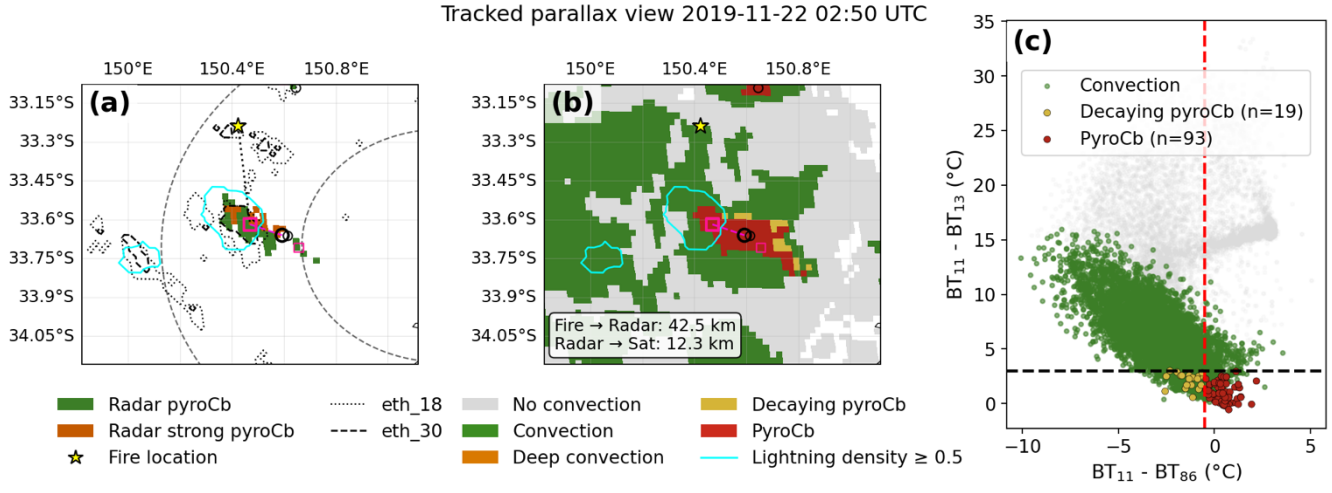

Figure 6. Example of multi-sensor tracking and classification of pyroconvection for the 22 November 2019 case at 02:50 UTC. (a) Radar-based view showing detected pyroCb features, including standard and strong pyroCb classifications (ETH10 > 8 km, and ETH10 > 10 km with persistent max (Z) > 10 dB), with echo-top height contours (ETH18 dotted, ETH30 dashed) and the fire location (yellow star). (b) Corresponding satellite-based classification, highlighting convective, deep convective, decaying pyroCb, and pyroCb regions, with lightning density (≥ 0.5 flashes km^{-2}) overlaid. The spatial offsets between the fire, radar, and satellite detections are indicated (Fire → Radar: 42.5 km; Radar → Satellite: 14.3 km). (c) Feature-space representation of satellite brightness temperature differences (BT_{11}– BT_{86} vs. BT_{11}– BT_{13}), illustrating the separation between convection (green), decaying pyroCb (yellow), and pyroCb (red), with threshold values shown as dashed lines. All identified objects are shown (pink squares for radar, black circles for satellite) but only the primary radar centroid and primary satellite centroids are used for tracking (shown with the largest squares and circles).

https://doi.org/10.5194/egusphere-2026-1907
Preprint. Discussion started: 18 May 2026

This case highlights the fundamental distinction between cloud-top and dynamical-core perspectives of pyroconvection. During the early phase, satellite and radar provide consistent representations of the developing system, capturing the onset of deep convection. In contrast, during the mature stage, the satellite classification increasingly reflects the evolution of the anvil rather than the underlying convective dynamics. The persistence and spatial expansion of class 4 detections illustrate the tendency of the satellite algorithm to retain advected or detached cloud-top structures as active pyroCb, even as radar signatures of deep convection weaken or remain spatially confined. This behaviour is consistent with the multi-event statistics presented in Section 3.3 and underscores the importance of distinguishing between active and residual stages of pyroconvective systems.

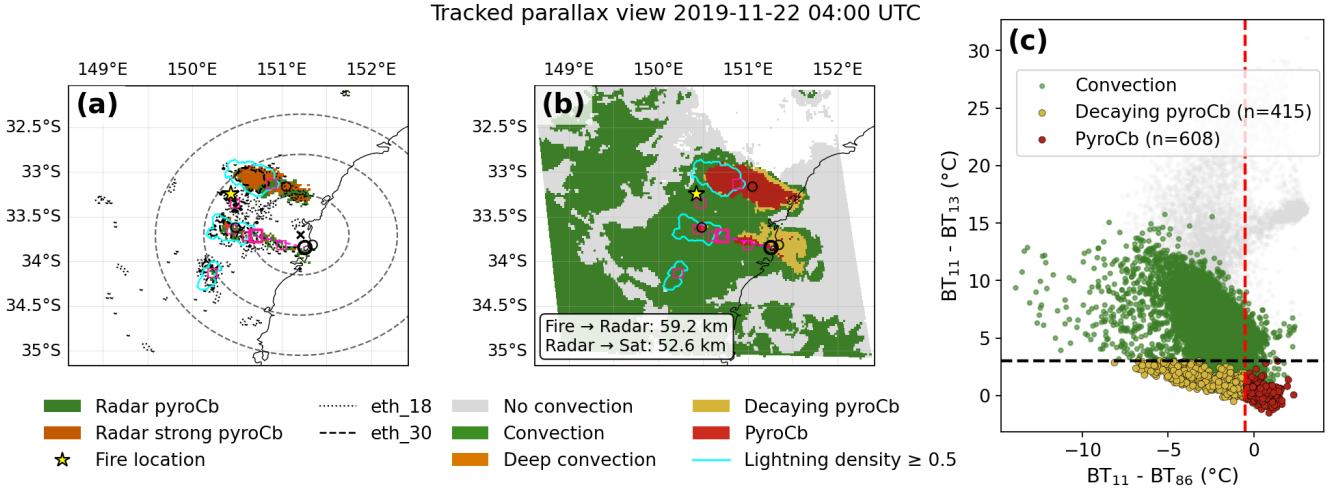

Figure 7. Same as Figure 6 but for timestamp 04:10 UTC.

3.2.2 Secondary case: Wulgulmerang, Victoria

The Wulgulmerang event (30 December 2019) provides a complementary example of pyroconvective evolution under conditions characterised by multiple convective elements and more complex spatial organisation. At the early stage (01:20 UTC; Fig. 8), radar observations reveal the presence of three compact convective cores exceeding deep convective thresholds, with echo-top heights indicative of vigorous vertical development. The satellite classification captures these features as regions of deep convection and pyroCb in close spatial proximity, with relatively small centroid displacement (~10–15 km), consistent with the behaviour observed in the primary case (first timestamp with both identification not shown but the reader can refer to later figures on multiple events statistics). Lightning activity is co-located with the convective cores, reinforcing the interpretation of active pyroconvection. In feature space, pixels associated with pyroCb again occupy the region defined by large shortwave–infrared brightness temperature differences and cold cloud-top temperatures, confirming the robustness of the microphysical discrimination.

https://doi.org/10.5194/egusphere-2026-1907
Preprint. Discussion started: 18 May 2026

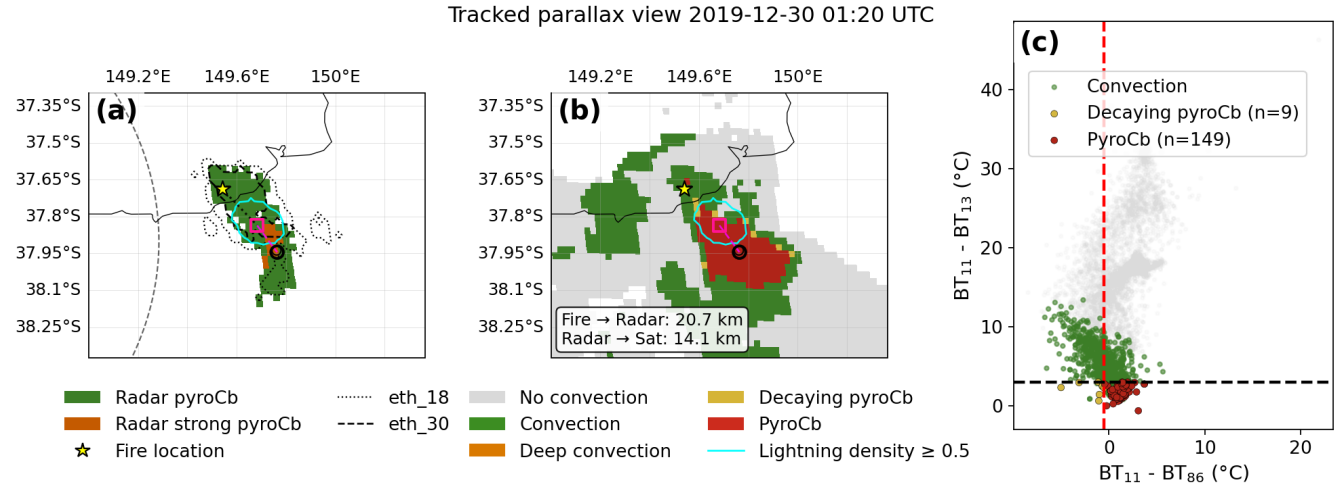

Figure 8. Same as Figure 6 but for the 30 December 2019 case at 01:20 UTC.

As the system evolves (06:20 UTC; Fig. 9), the spatial complexity increases, with radar observations showing multiple convective cells and a fragmented structure. In contrast, the satellite-derived classification exhibits a more continuous and expansive field, extending downwind and encompassing both active convective regions and broader anvil structures. This results in a marked increase in centroid displacement and a reduction in spatial agreement between radar and satellite objects. A substantial fraction of the satellite-detected area is classified as decaying pyroCb (class 4), forming elongated regions that are partially or fully detached from the radar-defined convective cores and associated lightning activity.

Compared to the Gospers Mountain case, the Wulgulmerang event emphasises the influence of structural complexity on radar–satellite discrepancies. While the initial detection of deep convection is consistent across both observational frameworks, the presence of multiple cells and their subsequent evolution enhances the divergence between the dynamical-core and cloud-top perspectives. The satellite classification tends to aggregate adjacent and advected cloud-top features into a single, coherent structure, whereas radar resolves discrete convective elements tied to active updrafts. This leads to an apparent overestimation of spatial extent and persistence in the satellite-derived pyroCb classification. As in the primary case, the increasing dominance of class 4 detections during the mature phase highlights the role of advected or detached anvils in driving the observed discrepancies, reinforcing the need to distinguish between active and residual stages of pyroconvective systems.

https://doi.org/10.5194/egusphere-2026-1907
Preprint. Discussion started: 18 May 2026

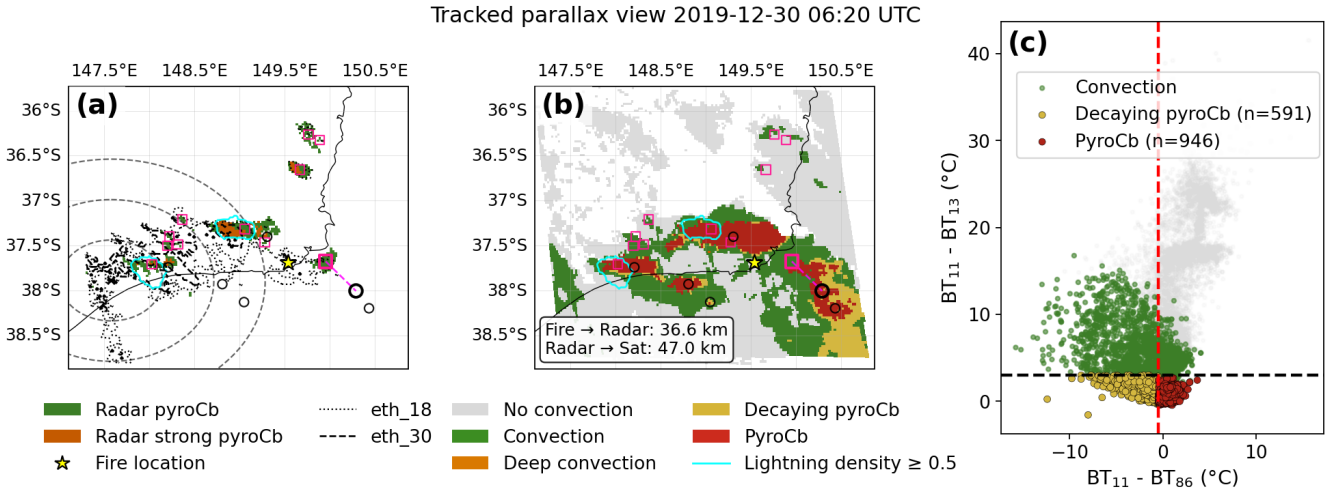

Figure 9. Same as Figure 6 but for the 30 December 2019 case at 06:20 UTC.

3.3 Multi-event statistics and timing of PyroCb detection

Figure 10 summarises the temporal evolution of radar- and satellite-derived pyroconvective object properties across all 8 analysed events, expressed relative to radar-defined onset. A consistent behaviour emerges across cases, characterised by strong agreement during the early development phase followed by progressive divergence at later times. Radar- and satellite-derived plume areas (Figs. 10a–b) exhibit similar magnitudes near onset, indicating that the satellite algorithm effectively captures the initial growth of deep convection. However, as time progresses, satellite-derived areas generally exceed those from radar (for 5 cases), reflecting the horizontal expansion and advection of the anvil cloud beyond the actively convecting core. For two cases (2019_VIC_GO, 2023_NSW_NY), the anvil clouds only appear briefly, due to deep convection not as sustained as for other events, therefore exhibiting satellite areas smaller than radar areas. The event 2019_VIC_WU also exhibits smaller satellite areas than radar areas for the first hour past onset but shows much larger areas past than onset period (not shown) supporting the general behavior observed for other events.

This divergence is further illustrated by the increase in centroid displacement (Fig. 10c), which remains small during the early phase but grows systematically with time, indicating a spatial decoupling between radar-observed convective cores and satellite-detected cloud-top structures. Consistently, the intersection-over-union (IoU; Fig. 10d) is highest near onset and decreases thereafter, confirming the reduction in spatial overlap between radar and satellite objects as the plume evolves. While some variability exists between events, the overall pattern is robust, highlighting a transition from strong radar–satellite agreement during initiation to increasing mismatch during the mature and decay stages. These results demonstrate that satellite-

https://doi.org/10.5194/egusphere-2026-1907
Preprint. Discussion started: 18 May 2026

based detection reliably captures the onset of pyroconvective activity but progressively represents advected anvil structures rather than the underlying convective dynamics. However, three events (first three rows of Figure 10b) exhibit 20 to 40 min delay in the onset detection compared to radar. This is likely due to the strength of deep convection and the time for it to reach the tropopause and form an anvil: weather radar will detect deep pyroconvection close to the tropopause earlier than satellite, before anvil formation. This has important consequences for operational monitoring and supports the benefit of a multi-sensor detection approach.

Comparing Figs. 10 and 11 highlights the impact of the satellite classification definition on object-based metrics. Restricting satellite objects to class 5 reduces both the spatial extent and temporal persistence of detected features, leading to improved agreement with radar during the early phase. However, the systematic divergence at later times remains, indicating that even the most restrictive cloud-top-based definition cannot fully capture the evolution of the dynamically active convective core.

https://doi.org/10.5194/egusphere-2026-1907
Preprint. Discussion started: 18 May 2026

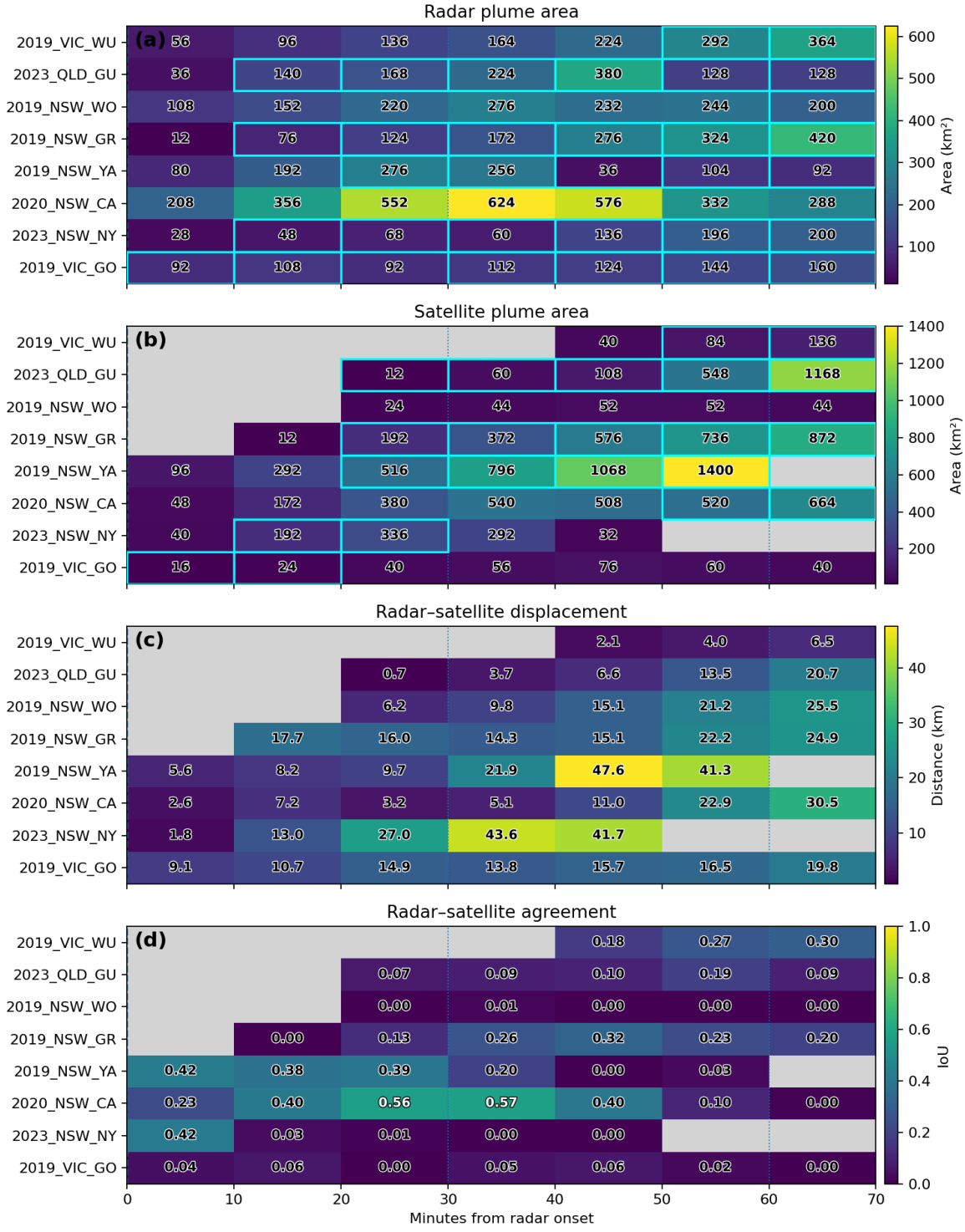

490

https://doi.org/10.5194/egusphere-2026-1907
Preprint. Discussion started: 18 May 2026

Figure 10. Time-resolved comparison of radar (class 1 and 2) and satellite pyroconvective objects (class 4 and 5) across all events. Each row represents an individual event, and columns show time relative to radar-defined onset (minutes). (a) Radar plume area. (b) Satellite plume area. (c) Radar–satellite centroid displacement (km). (d) Intersection-over-union (IoU) between object masks. Colours indicate the magnitude of each metric, with grey cells denoting missing data. The systematic increase in displacement and decrease in IoU with time illustrates the growing decoupling between convective cores and advected anvil structures. Occurrence of lightning within the radar or satellite centroids is indicated by the cyan contour for each cell of the table in (a) and (b).

Figure 12 illustrates the trajectories of radar- and satellite-derived pyroconvective object centroids for selected events, providing a Lagrangian perspective on the evolution of plume position. At early times, radar and satellite centroids follow similar paths, consistent with the strong spatial agreement observed near onset (Fig. 11). As the events evolve, however, the satellite-derived tracks progressively diverge from the radar-derived trajectories, with increasing separation in both magnitude and direction. This divergence reflects the advection of the anvil cloud by the ambient flow, while the radar-observed convective core remains more closely tied to the source region of active updrafts. We shall note that the radar tracks at +30 min after onset for 2020_NSW_CA and 2023_QLD_GU are not reliable as the radar object is discontinued in space because of a split and therefore the centroid is artificially tracking back from the initial trajectory. For 2023_QLD_GU, the radar object is also becoming a very large object, therefore the centroid is more variable from timestamp to timestamp than for a smaller object. However, the observed slow motion of the radar object is well respected.

The separation between tracks is particularly pronounced during the mature stage, where satellite centroids can be displaced tens of kilometres from the radar-defined convective core. In some cases, the satellite track continues to evolve smoothly even as the radar signal weakens or becomes fragmented, indicating that the detected object is dominated by residual cloud-top structures rather than active convection. These results are consistent with the temporal evolution shown in Fig. 10-11 and further demonstrate that satellite-based tracking increasingly follows advected anvil features rather than the dynamically active plume. The track-based representation therefore provides a complementary view of the systematic decoupling between cloud-top and convective-core perspectives of pyroconvective systems. We note that all tracks corresponding to the early to intermediate stage of pyroCb development for these 8 events show west to east trajectories, in line with what is commonly observed for standard thunderstorms on the East Coast of Australia.

https://doi.org/10.5194/egusphere-2026-1907
Preprint. Discussion started: 18 May 2026

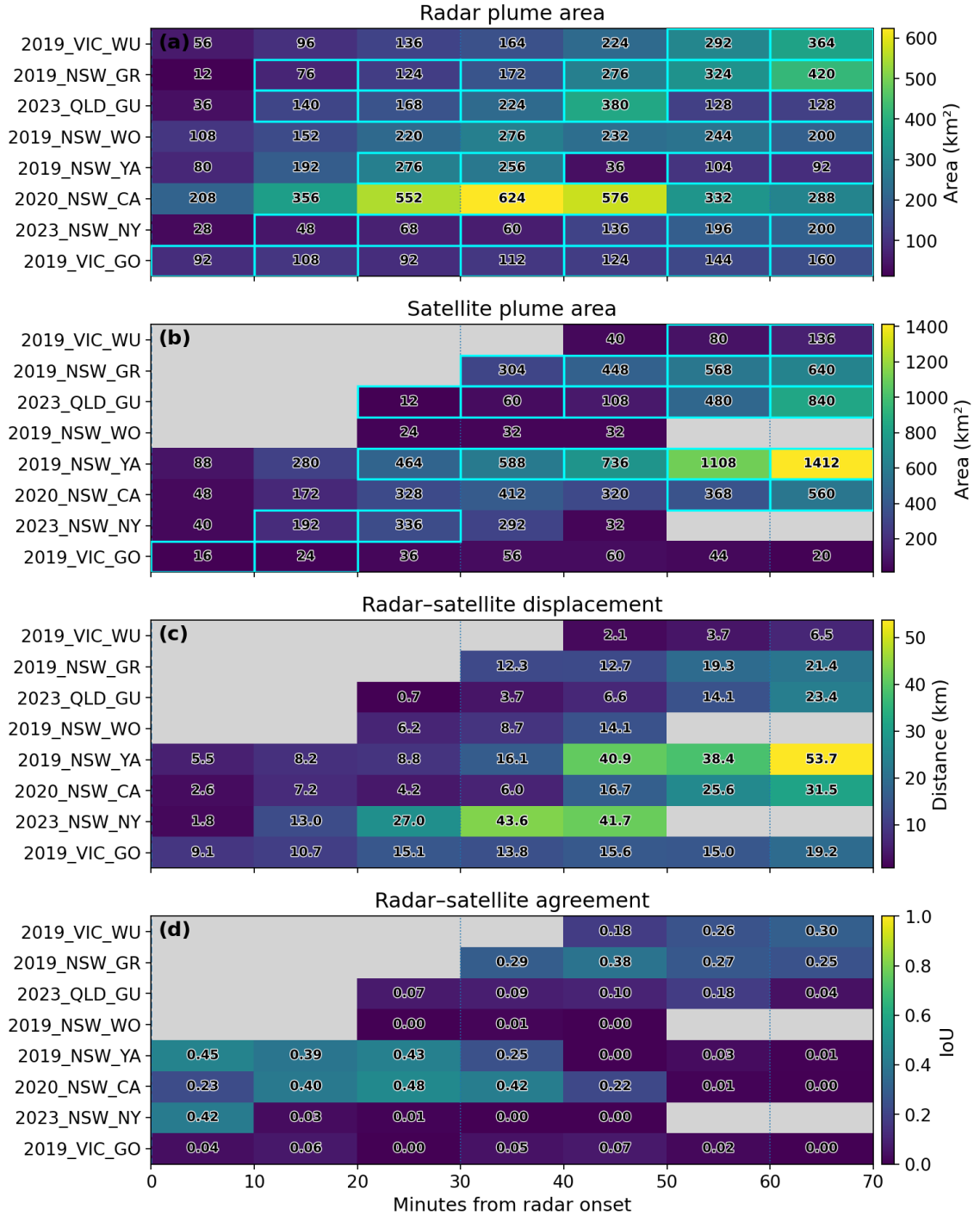

Figure 11. same as Fig. 10 but using satellite class 5 only (excluding decaying anvils).

https://doi.org/10.5194/egusphere-2026-1907
Preprint. Discussion started: 18 May 2026

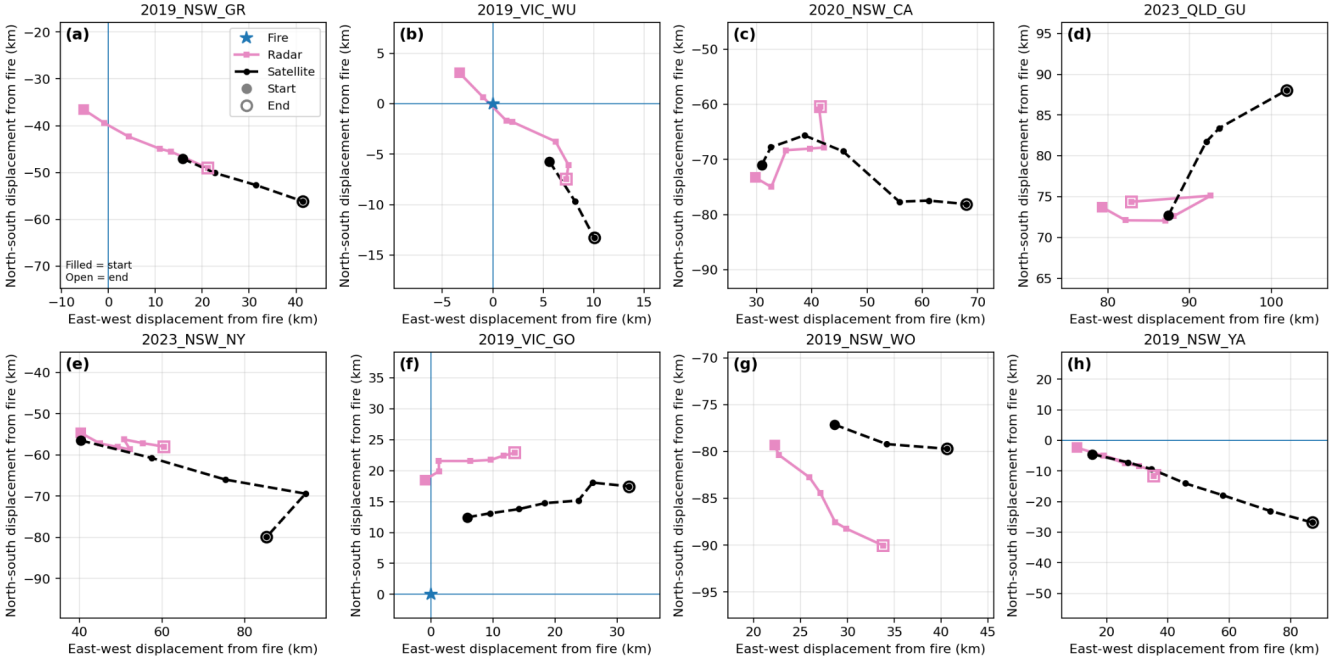

Figure 12. Tracks of pyroconvective objects derived from radar and satellite observations (filled symbols correspond to the onset - earliest observations for each sensor, while open symbols correspond to onset + 60 min). Radar centroids (pink lines) and satellite centroids (black dashed lines) are shown for each event, with markers indicating time progression. Early-stage trajectories are closely aligned, while increasing separation at later times illustrates the displacement of satellite-detected anvils relative to the radar-observed convective core.

4. Discussion

4.1 PyroCb definition and early-phase agreement

Pyrocumulonimbus (pyroCb) can be defined from two complementary perspectives: a dynamical perspective, in which pyroCb correspond to deep fire-driven convection characterised by strong updrafts and electrification, and a satellite-based perspective, in which they are identified through cold cloud-top temperatures and anvil signatures. This distinction is central to interpreting the results of this study.

During the early phase of pyroconvective development, satellite-derived classifications show strong agreement with radar-based indicators of deep convection, including echo-top heights and lightning activity albeit noting that for three tracked cases studied out of eight, the lag can be from 20 min to 40 min to capture the onset. The hypothesis for this lag relates to the nature and strength of deep pyroconvection for these events. Overall, the perfect agreement for other cases reflects the close coupling

https://doi.org/10.5194/egusphere-2026-1907
Preprint. Discussion started: 18 May 2026

between the cloud-top signal and the actively rising convective core at initiation. At this stage, the anvil has not yet fully developed or detached from the updraft, and satellite observations provide a reliable proxy for deep convective intensity and timing.

4.2 Progressive divergence and physical interpretation

As events evolve, a systematic divergence emerges between satellite- and radar-derived representations of pyroconvection. Satellite-derived objects increasingly capture horizontally advected anvil structures, while radar observations continue to track the actively convecting core. This behaviour is reflected in increasing centroid displacement, decreasing spatial overlap, and an apparent overestimation of plume extent and persistence in satellite retrievals.

This divergence highlights a fundamental limitation of satellite-based detection approaches: they primarily sample cloud-top and anvil properties rather than the underlying convective dynamics. As a result, detached or decaying anvils may be interpreted as ongoing deep convection, even when radar observations indicate weakening or cessation of updraft activity. The persistence of such “orphan anvils” introduces a systematic bias in satellite-based assessments of pyroCb duration and spatial extent.

4.3 Implications for detection, tracking, and cloud-top dynamics

These results have important implications for the detection and tracking of pyroCb in both research and operational contexts. Satellite-based algorithms, including those derived from the P17 framework, are effective for identifying the onset of deep pyroconvection but may overestimate the duration and spatial extent of events during later stages. In contrast, radar observations provide a more direct measure of convective intensity but are spatially limited and not always available.

Recent studies have demonstrated that cloud-top motion derived from geostationary satellite imagery can capture aspects of pyroCb dynamics using optical flow techniques, including the identification of convective pulses and temporal variability in updraft strength (McHardy et al., 2024). These results indicate that satellite observations contain a dynamical signal, albeit at the level of the cloud top. The present analysis shows that this signal becomes increasingly decoupled from the underlying convective core as the anvil expands and advects. Consequently, satellite-derived diagnostics should be interpreted as representing the evolution of the cloud-top and anvil structure rather than a direct measure of deep convective intensity.

The object-based tracking framework used in this study provides a quantitative means of characterising these differences through metrics such as spatial overlap, centroid displacement, and area evolution. While effective for diagnosing the geometric evolution of pyroCb features, these metrics do not explicitly capture the temporal variability of convective intensity. Integrating cloud-top motion diagnostics or temporal gradients of satellite and radar fields may provide a more complete description of pyroCb dynamics.

https://doi.org/10.5194/egusphere-2026-1907
Preprint. Discussion started: 18 May 2026

4.4 A dual-perspective framework for pyroCb observations

Overall, the results support a conceptual framework in which pyroCb observations can be interpreted through two complementary perspectives: (i) a cloud-top perspective, provided by satellite observations, which captures the evolution of the anvil and upper-level plume, and (ii) a dynamical-core perspective, provided by radar and lightning observations, which captures the actively convecting region.

Discrepancies between these perspectives are therefore not inconsistencies but reflect different components of the pyroconvective system. Integrating these perspectives is essential for accurately characterising the full lifecycle of pyroCb, including initiation, growth, and decay phases.

5. Conclusion

In this study, we evaluated a satellite-based pyroCb detection algorithm in the Australian context using a multi-sensor framework combining geostationary satellite observations, weather radar, and lightning data. By integrating these complementary datasets within the PyroScope platform, we were able to assess not only the timing and spatial extent of satellite-derived pyroconvective classifications, but also their physical consistency with dynamically active convection. The results demonstrate that satellite-based detection reliably captures the onset of deep pyroconvective development, with strong agreement with radar-derived echo-top heights and lightning activity during the early phase. However, a systematic divergence emerges as events evolve, with satellite classifications increasingly dominated by advected and persistent anvil structures rather than the underlying convective core. This behaviour reflects a fundamental limitation of cloud-top-based detection frameworks and highlights the importance of distinguishing between active and residual stages of pyroconvection.

The introduction of an additional spectral test to separate detached anvils (class 4) from intense pyroCb (class 5) provides a partial mitigation of this limitation and enables a more physically meaningful interpretation of satellite-derived classifications. Nevertheless, the results emphasise that no single observational framework can fully capture the complexity of pyroconvective systems, and that multi-sensor approaches are essential for robust detection and analysis.

Several avenues for future work emerge from this study. First, the current object-based tracking framework relies on a simple nearest-neighbour association and does not explicitly account for the complex behaviour of pyroconvective systems, including object splitting, merging, and interaction between multiple convective cells. Extending the methodology to handle such complex multi-object configurations will be critical for analysing realistic wildfire events, particularly those characterised by clustered or rapidly evolving convection. Second, the present analysis focuses on well-defined pyroCb cases with strong signals, whereas events with weak or marginal signatures, as well as cases that do not develop into pyroCb, remain largely unexplored. Including these events will be essential to assess detection skill, false positives, and the conditions under which pyroconvection fails to intensify.

https://doi.org/10.5194/egusphere-2026-1907
Preprint. Discussion started: 18 May 2026

Third, the analysis presented here is intentionally restricted to the early development phase, where object tracking is most robust and radar–satellite agreement is strongest. Extending the tracking framework to the mature and decay phases of pyroconvective systems will allow a more complete characterisation of plume evolution, including the transition from active convection to residual anvil structures. This will require more advanced tracking strategies capable of handling fragmentation, dissipation, and increasing spatial decoupling between observational perspectives.

Ultimately, the development of robust, multi-sensor object tracking provides a pathway toward a quantitative, lifecycle-based understanding of pyroconvection. By enabling consistent tracking of pyroCb from initiation through maturity to decay, such approaches will support the derivation of metrics describing growth, intensity, duration, and spatial evolution. In addition, extending the analysis to pre-onset conditions offers the potential to identify precursors to pyroCb formation, linking environmental forcing and fire behaviour to the emergence of deep convection. These advances will be essential for improving both the physical understanding and the operational monitoring of extreme wildfire–atmosphere interactions.

This distinction between cloud-top detection and convective dynamics provides a unifying framework for interpreting satellite-based pyroCb climatologies and for guiding the development of next-generation, multi-sensor detection algorithms.

Code and data availability

Implementation of the original P17 algorithm was initiated by LSF and later JV as part of internships at The University of Queensland and at The Australian Bureau of Meteorology. Subsequently, AG designed and created a platform to gather all sources of data and implement algorithms, under the name DASHFIRE to more broadly support satellite and radar-based algorithm development. The software PyroScope was developed from the ground up by AG in February–March 2026 to address structural limitations identified in the DASHFIRE framework. The Pyroscope software remains the intellectual property of the author and is not currently available in the public domain.

Author contributions

AG, JV and LSF analysed the data. All co-authors provided regular scientific inputs on the analysis. AG prepared the original manuscript with contributions from all co-authors.

Competing interests

The contact author has declared that neither they nor their co-authors have any competing interests.

https://doi.org/10.5194/egusphere-2026-1907
Preprint. Discussion started: 18 May 2026

Data accessibility

The operational weather radar data is freely available at https://www.openradar.io [last accessed 9 April 2026]. BARRA2 data are accessible on the NCI (https://opus.nci.org.au/pages/viewpage.action?pageId=264241166) [last accessed 9 April 2026]. Satellite data and products are accessible on the NCI through the BOM Satellite data collection (https://dx.doi.org/10.25914/5QRS-QB54) [last accessed 9 April 2026]. Lightning data is available upon request to the Weather Zone.

Acknowledgements

This research is directly supported by *Google.org*, the non-profitable branch of Google. This project was undertaken with the assistance of resources from the Australian National Computational Infrastructure (NCI) and the Australian Bureau of Meteorology, both of which are supported by the Australian Government. The open-source libraries Pandas (Pandas development team, 2010), Numpy (Van der Walt et al., 2011), Scipy (Virtanen et al., 2019), matplotlib (Hunter, 2007), Proplot (Davis, 2021), Pyart (Helmus and Collis, 2016), netCDF4 (Rew and Davis, 1990), scikit-learn (Pedregosa et al., 2011), in the Python programming language (Rossum, 1995) were used to develop and implement the code to process the data. The authors are thankful to Leon Majewksi, Vincent Villani and Caroline Poulsen for their advice on implementing the parallax correction and their work on making Himawari-8 data and cloud products available on the NCI. AI tools (Large Language Models) have been used to generate Figure 1 and to improve the grammar and check for spellings in the manuscript.

Disclaimer

Copernicus Publications remains neutral with regard to jurisdictional claims made in the text, published maps, institutional affiliations, or any other geographical representation in this paper. While Copernicus Publications makes every effort to include appropriate place names, the final responsibility lies with the authors. Views expressed in the text are those of the authors and do not necessarily reflect the views of the publisher.

References

Bessho, K., Date, K., Hayashi, M., Ikeda, A., Imai, T., Inoue, H., Kumagai, Y., Miyakawa, T., Murata, H., Ohno, T. and Okuyama, A., 2016. An introduction to Himawari-8/9—Japan's new-generation geostationary meteorological satellites. *Journal of the Meteorological Society of Japan. Ser. II*, *94*(2), pp.151-183. https://doi.org/10.2151/jmsj.2016-009

https://doi.org/10.5194/egusphere-2026-1907
Preprint. Discussion started: 18 May 2026

Bowman DMJS, Williamson GJ, Price OF, Ndalila MN, Bradstock RA. Australian forests, megafires and the risk of dwindling carbon stocks. *Plant Cell Environ*. 2021; 44: 347–355. https://doi.org/10.1111/pce.13916

Byrne, B., Liu, J., Lee, M., Yin, Y., Bowman, K. W., Miyazaki, K., et al. (2021). The carbon cycle of southeast Australia during 2019–2020: Drought, fires, and subsequent recovery. *AGU Advances*, 2, e2021AV000469. https://doi.org/10.1029/2021AV000469

Couto, F.T., Filippi, J.B., Baggio, R., Campos, C. and Salgado, R., 2024. Numerical investigation of the Pedrógão Grande pyrocumulonimbus using a fire to atmosphere coupled model. *Atmospheric Research*, *299*, p.107223.

Duff, T.J., Chong, D.M. and Penman, T.D., 2018. Quantifying wildfire growth rates using smoke plume observations derived from weather radar. *International journal of wildland fire*, *27*(8), pp.514-524.

Fromm, M., Servranckx, R., Stocks, B.J. *et al.* Understanding the critical elements of the pyrocumulonimbus storm sparked by high-intensity wildland fire. *Commun Earth Environ* **3**, 243 (2022). https://doi.org/10.1038/s43247-022-00566-8

Guyot, A., Brook, J. P., Protat, A., Turner, K., Soderholm, J., McCarthy, N. F., and McGowan, H.: Segmentation of polarimetric radar imagery using statistical texture, Atmos. Meas. Tech., 16, 4571–4588, https://doi.org/10.5194/amt-16-4571-2023, 2023.

McHardy, T. M., Peterson, D. A., Apke, J. M., Miller, S. D., Campbell, J. R., & Hyer, E. J. (2024). Novel comparison of pyrocumulonimbus updrafts to volcanic eruptions and supercell thunderstorms using optical flow techniques. Journal of Geophysical Research: Atmospheres, 129, e2023JD039418. https://doi.org/10.1029/2023JD039418

Inoue, T. (1987), A cloud type classification with NOAA 7 split-window measurements, J. Geophys. Res., 92(D4), 3991–4000, doi:10.1029/JD092iD04p03991.

Kablick III, G.P., Allen, D.R., Fromm, M.D. and Nedoluha, G.E., 2020. Australian pyroCb smoke generates synoptic-scale stratospheric anticyclones. *Geophysical Research Letters*, *47*(13), p.e2020GL088101.

Kaplan, J. O. and Lau, K. H.-K. 2022: World Wide Lightning Location Network (WWLLN) Global Lightning Climatology (WGLC) and time series, 2022 update, *Earth System Science Data*, 14, 5665–5670, https://doi.org/10.5194/essd-14-5665-2022.

https://doi.org/10.5194/egusphere-2026-1907
Preprint. Discussion started: 18 May 2026

Kerdraon, G., Fontaine, E. (2021). Algorithm Theoretical Basis Document for the Cloud Product Processors of the NWC/GEO https://opus.nci.org.au/download/attachments/206110974/NWC-CDOP3-GEO-MFL-SCI-ATBD-Cloud_v1.0.1.pdf?version=1&modificationDate=1676263629164&api=v2 [last accessed 31 October 2024].

Krishna, M., Saide, P. E., Ye, X., Turney, F. A., Hair, J. W., Fenn, M., & Shingler, T. (2024). Evaluation of wildfire plume injection heights estimated from operational weather radar observations using airborne Lidar retrievals. *Journal of Geophysical Research: Atmospheres*, 129, e2023JD039926. https://doi.org/10.1029/2023JD039926

Lakshmanan, V., Hondl, K., Potvin, C. K. & Preignitz, D. An Improved Method for Estimating Radar Echo-Top Height. Weather Forecast. 28, 481–488 (2013).

Lang, T., Dolan, B., Guy, N., Gerlach, C.A.M., Hardin, J. & Raut, B. (2024). CSU-Radarmet/CSU_RadarTools: CSU_RadarTools v1.4 (v1.4). Zenodo. https://doi.org/10.5281/zenodo.13975472

Lareau Neil P., Clements Craig B., Kochanski Adam, Aydell Taylor, Hudak Andrew T., McCarley T. Ryan, Ottmar Roger (2024) Observations of a rotating pyroconvective plume. *International Journal of Wildland Fire* 33, WF23045. https://doi.org/10.1071/WF23045

May, R. M., Goebbert, K. H., Thielen, J. E., Leeman, J. R., Camron, M. D., Bruick, Z., Bruning, E. C., Manser, R. P., Arms, S. C., and Marsh, P. T., 2022: MetPy: A Meteorological Python Library for Data Analysis and Visualization. *Bull. Amer. Meteor. Soc.*, **103**, E2273-E2284, https://doi.org/10.1175/BAMS-D-21-0125.1.

McHardy, T. M., Peterson, D. A., Apke, J. M., Miller, S. D., Campbell, J. R., & Hyer, E. J. (2024). Novel comparison of pyrocumulonimbus updrafts to volcanic eruptions and supercell thunderstorms using optical flow techniques. *Journal of Geophysical Research: Atmospheres*, 129, e2023JD039418. https://doi.org/10.1029/2023JD039418

McCarthy, N., Guyot, A., Dowdy, A., and McGowan, H.: Wildfire and weather radar: A review. Journal of Geophysical Research: Atmospheres, 124(1), 266– 286. https://doi.org/10.1029/2018JD029285, 2019.

McRae R. (2025). Australia PyroCb Register, February 2025. Published on-line at: https://www.highfirerisk.com.au/pyrocb/register.htm

https://doi.org/10.5194/egusphere-2026-1907
Preprint. Discussion started: 18 May 2026

McRae, R.H., Sharples, J.J. and Fromm, M., 2015. Linking local wildfire dynamics to pyroCb development. *Natural Hazards and Earth System Science*, *15*(3), pp.417-428.

Nolan, R. H., Bowman, D. M. J. S., Clarke, H., Haynes, K., Ooi, M. K. J., Price, O. F., Williamson, G. J., Whittaker, J., Bedward, M., Boer, M. M., Cavanagh, V. I., Collins, L., Gibson, R. K., Griebel, A., Jenkins, M. E., Keith, D. A., Mcilwee, A. P., Penman, T. D., Samson, S. A., ... Bradstock, R. A. (2021). What Do the Australian Black Summer Fires Signify for the Global Fire Crisis? *Fire*, *4*(4), 97. https://doi.org/10.3390/fire4040097

Ohneiser, K., Ansmann, A., Kaifler, B., Chudnovsky, A., Barja, B., Knopf, D. A., Kaifler, N., Baars, H., Seifert, P., Villanueva, D., Jimenez, C., Radenz, M., Engelmann, R., Veselovskii, I., and Zamorano, F.: Australian wildfire smoke in the stratosphere: the decay phase in 2020/2021 and impact on ozone depletion, Atmos. Chem. Phys., 22, 7417–7442, https://doi.org/10.5194/acp-22-7417-2022, 2022.

Peace, M., McCaw, L., Santos, B., Kepert, J.D., Burrows, N. and Fawcett, R.J., 2017. Meteorological drivers of extreme fire behaviour during the Waroona bushfire, Western Australia, January 2016. *Journal of Southern Hemisphere Earth Systems Science*, *67*(2), pp.79-106.

Peterson, D.A., Fromm, M.D., Solbrig, J.E., Hyer, E.J., Surratt, M.L. and Campbell, J.R., 2017a. Detection and inventory of intense pyroconvection in western North America using GOES-15 daytime infrared data. *Journal of Applied Meteorology and Climatology*, *56*(2), pp.471-493.

Peterson, D.A., Hyer, E.J., Campbell, J.R., Solbrig, J.E. and Fromm, M.D., 2017b. A conceptual model for development of intense pyrocumulonimbus in western North America. *Monthly Weather Review*, *145*(6), pp.2235-2255.

Peterson, D.A., Fromm, M.D., McRae, R.H., Campbell, J.R., Hyer, E.J., Taha, G., Camacho, C.P., Kablick III, G.P., Schmidt, C.C. and DeLand, M.T., 2021. Australia's Black Summer pyrocumulonimbus super outbreak reveals potential for increasingly extreme stratospheric smoke events. *NPJ climate and atmospheric science*, *4*(1), p.38.

Peterson, D.A., Thapa, L.H., Saide, P.E., Soja, A.J., Gargulinski, E.M., Hyer, E.J., Weinzierl, B., Dollner, M., Schöberl, M., Papin, P.P. and Kondragunta, S., 2022. Measurements from inside a thunderstorm driven by wildfire: The 2019 FIREX-AQ field experiment. *Bulletin of the American Meteorological Society*, *103*(9), pp.E2140-E2167.

Potter, B.E., 2012. Atmospheric interactions with wildland fire behaviour–I. Basic surface interactions, vertical profiles and synoptic structures. *International Journal of Wildland Fire*, *21*(7), pp.779-801.

https://doi.org/10.5194/egusphere-2026-1907
Preprint. Discussion started: 18 May 2026

Potter, B.E., 2012. Atmospheric interactions with wildland fire behaviour–II. Plume and vortex dynamics. *International Journal of Wildland Fire*, *21*(7), pp.802-817.

Price, O.F., Purdam, P.J., Williamson, G.J. and Bowman, D.M., 2018. Comparing the height and area of wild and prescribed fire particle plumes in south-east Australia using weather radar. *International journal of wildland fire*, *27*(8), pp.525-537.

Raspaud, M., Hoese, D., Lahtinen, P., & Dybbroe, A. (2025). Pytroll/satpy: vX.Y.Z (Version vX.Y.Z). Zenodo. https://zenodo.org/badge/latestdoi/51397392

Rosenfeld, D., M. Fromm, J. Trentmann, G. Luderer, M. O. Andreae, and R. Servranckx, 2007: The Chisholm firestorm: Observed microstructure, precipitation and lightning activity of a pyro-cumulonimbus. *Atmos. Chem. Phys.*, **7**, 645–659, doi:10.5194/acp-7-645-2007.

Schwartz, M. J., Santee, M. L., Pumphrey, H. C., Manney, G. L., Lambert, A., Livesey, N. J., et al. (2020). Australian new year's pyroCb impact on stratospheric composition. *Geophysical Research Letters*, 47, e2020GL090831. https://doi.org/10.1029/2020GL090831

Strabala, K. I., S. A. Ackerman, and W. P. Menzel, 1994: Cloud Properties inferred from 812-µm Data. *J. Appl. Meteor. Climatol.*, **33**, 212–229, https://doi.org/10.1175/1520-0450(1994)033<0212:CPIFD>2.0.CO;2.

Su, C.-H., Rennie, S., Dharssi, I., Torrance, J., Smith, A., Le, T., Steinle, P., Stassen, C., Warren, R. A., Wang, C., and Le Marshall, J. (2022), BARRA2: Development of the next-generation Australian regional atmospheric reanalysis, Bureau Research Report 067, accessed online http://www.bom.gov.au/research/publications/researchreports/BRR-067.pdf

Su, C.-H., Torrance, J., Rennie, S., Dharssi, I., Tian, S., Howard, E., Pepler, A., Stassen, C., Steinle, P. (2023), Preliminary assessment of regional moderate-resolution atmospheric reanalysis for Australia, Bureau Research Report 084, accessed online http://www.bom.gov.au/research/publications/researchreports/BRR-084.pdf

Tessendorf, S. A., Miller, L. J., Wiens, K. C., & Rutledge, S. A. (2005). The 29 June 2000 supercell observed during STEPS. Part I: Kinematics and microphysics. Journal of the Atmospheric Sciences, 62(12), 4127-4150.

Terrasson, A., McCarthy, N., Dowdy, A., Richter, H., McGowan, H. and Guyot, A., 2019. Weather radar insights into the turbulent dynamics of a wildfire-triggered supercell thunderstorm. *Journal of Geophysical Research: Atmospheres*, *124*(15), pp.8645-8658.

https://doi.org/10.5194/egusphere-2026-1907
Preprint. Discussion started: 18 May 2026

Tory, K. J., and J. D. Kepert, 2021: Pyrocumulonimbus Firepower Threshold: Assessing the Atmospheric Potential for pyroCb. *Wea. Forecasting*, **36**, 439–456, https://doi.org/10.1175/WAF-D-20-0027.1.

Xu, W., Wooster, M.J., Kaneko, T., He, J., Zhang, T. and Fisher, D., 2017. Major advances in geostationary fire radiative power (FRP) retrieval over Asia and Australia stemming from use of Himarawi-8 AHI. *Remote Sensing of Environment*, *193*, pp.138-149.

Zhu, Y., Stock, M., Lapierre, J. and DiGangi, E. 2022. "Upgrades of the Earth Networks Total Lightning Network in 2021" *Remote Sensing* 14, no. 9: 2209. https://doi.org/10.3390/rs14092209